Cross sections for $(n,2n)$ and $(n,3n)$ reactions above 14 MeV†

L. R. Veeser, E. D. Arthur, and P. G. Young
Los Alamos Scientific Laboratory, University of California, Los Alamos, New Mexico 87545
(Received 2 May 1977)

Cross sections for $(n,2n)$ and $(n,3n)$ reactions have been measured between 14.7 and 24.0 MeV using a large liquid scintillator to detect neutrons. Measurements were made for ^{45}Sc, ^{59}Co, ^{89}Y, ^{93}Nb, ^{103}Rh, ^{169}Tm, ^{175}Lu, ^{181}Ta, ^{197}Au, and ^{209}Bi samples. The excitation functions are compared with calculations based on a statistical, preequilibrium model using global sets of optical model and level density parameters.

[NUCLEAR REACTIONS ^{45}Sc$(n,2n)$; ^{59}Co$(n,2n),(n,3n)$; ^{89}Y$(n,2n),(n,3n)$; ^{93}Nb$(n,2n),(n,3n)$; ^{103}Rh$(n,2n),(n,3n)$; ^{169}Tm$(n,2n),(n,3n)$; ^{175}Lu$(n,2n),(n,3n)$; ^{181}Ta$(n,2n),(n,3n)$; ^{197}Au$(n,2n),(n,3n)$; ^{209}Bi$(n,2n),(n,3n)$; $E=14.7$–24.0 MeV, measured $\sigma(E)$, calculated $\sigma(E)$. Natural targets.]

I. INTRODUCTION

Cross sections for $(n,2n)$ and $(n,3n)$ reactions have usually been measured by radiochemical techniques; a sample is activated in a known, monoenergetic neutron flux and cross sections are determined from the induced activity of the residual nuclei. To measure $(n,2n)$ cross sections for samples without radioactive reaction products, Ashby *et al*[1] used a large tank filled with liquid scintillator to detect the emitted neutrons. Recently, scintillator-tank methods have been improved and extended to many nuclei for energies from threshold up to 15 MeV.[2,3] We report scintillator-tank measurements of $(n,2n)$ and $(n,3n)$ cross sections from 14.7 to 24.0 MeV for 10 elements, several of which have recently been investigated radiochemically in this energy region.[4]

II. EXPERIMENT

The method used to make the measurements is very similar to that used by Fréhaut and Mosinski[3] and described in detail in Ref. 5. Figure 1 shows a schematic of the experiment. A sample was placed at the center of a large, gadolinium-loaded liquid scintillator where it was irradiated by a pulsed beam of monoenergetic neutrons. If an $(n,2n)$ or $(n,3n)$ event occurred during the pulse, it was identified by two or three separate pulses from the scintillator.

A. Neutron source

A beam of deuterons from the Los Alamos Scientific Laboratory vertical Van de Graaff accelerator struck the tritium gas in a 3-cm-long cell to produce the high-energy neutrons. A large iron shield partially surrounded the gas cell to reduce the intensity of background neutrons in the room. Neutrons emerging at 0° were collimated by a 75-cm-long brass cylinder with a tapered hole subtending a half-angle of 1.0°. The tritium, at pressures of up to 2.2 atm, was contained in the cell by a 5.3-mg/cm^2 molybdenum entrance foil sealed with indium gaskets. For the 14.7-MeV neutron case, the deuterons emerging from the foil and entering the tritium had an energy of 130 keV and stopped in the gas. Although the 0° neutrons ranged from 14.1 to 14.85 MeV, nearly all of them had energies above 14.55 MeV. For higher energy measurements, the deuterons stopped in a gold beam stop that formed the end of the cell, and the neutron energy was calculated at the cell center. Most of the neutron energy spread resulted from the variation in deuteron energy in the cell.

B. Beam monitor

The neutron beam intensity was measured by a 5.1-cm-long by 5.1-cm-diam cylinder of liquid scintillator (Nuclear Enterprises type NE-213) used as a monitor detector. The monitor was placed in the beam behind the sample and the tank about 4.2 m from the neutron source. The pulse height spectrum was recorded for each run, and the neutron flux was found by relating the height and the end point of the plateau from the recoil protons to the absolute differential efficiency measurements of Verbinski.[6] γ-ray pulse shape discrimination proved unnecessary. The method provided an absolute flux determination with an estimated accuracy of better than 5%.

Since our accelerator does not have the capability of time-of-flight pulsing to determine the incident neutron spectra, we avoided counting low-en-

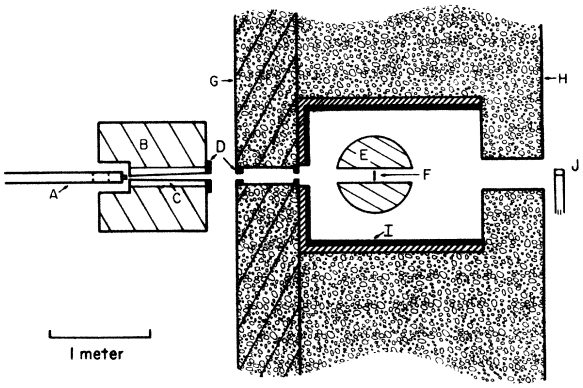

FIG. 1. The experimental arrangement: (A) accelerator beam tube, collimator, and tritium cell; (B) iron shield; (C) brass neutron collimator; (D) boron shielding; (E) scintillator tank; (F) sample; (G) magnetite concrete shielding; (H) gypsum shielding; (I) borax and lead shielding layers; (J) neutron monitor detector.

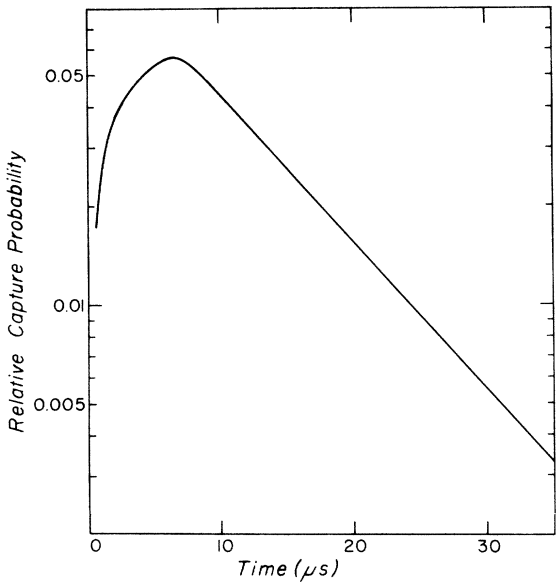

FIG. 2. Measured probability of neutron capture in the liquid scintillator tank versus the time after entering the tank.

ergy neutrons from deuteron breakup and d-^{2}H reactions from deuterium contaminants in the beam line and target by using only the upper part of the monitor spectrum. The low-energy neutrons could produce pulse heights up to about 30% of the maximum from d-^{3}H neutrons, and the monitor threshold was set at about 60%.

The low-energy neutrons were usually below the threshold for the $(n,2n)$ reaction. For measurements at 23 and 24 MeV, some samples had $(n,2n)$ thresholds exceeded by the d-^{2}H energy, but the contribution to the cross section was disregarded because of large $(n,2n)$ uncertainties for these samples relative to the maximum possible d-^{2}H effect. Thus the only major effect of the low-energy neutrons was scattering in the sample, thereby increasing the multiple events correction (see Sec. III).

C. Neutron detector

The neutron detector is a 75-cm-diam spherical tank with a 15-cm-diam hole through the center for the neutron beam. A thick shield wall surrounding the tank has holes for the neutron beam to enter and exit. The tank is filled with 200 liters of liquid scintillator (Nuclear Enterprises type NE-323 loaded with 0.5-wt% gadolinium). Eight photomultiplier tubes (type RCA-4522) are mounted on windows in the tank walls. Anode signals from the tubes were added together in two banks of four tubes each, and a light pulse in the tank was identified by a signal coincidence between the two banks. The sample was placed at the center of the tank, 2.6 m from the source.

Neutrons emitted by the sample entered the tank, thermalized in the liquid, and either escaped or were captured. By observing the capture γ rays and knowing the detector efficiency, we could determine the number of neutrons that entered the tank. The amount of gadolinium in the liquid is large enough to capture most of the neutrons, but small enough so that the captures occurred over a range of times and could be counted individually. Figure 2 shows the relative capture probability for the detector as a function of time. After a tank pulse the deadtime of the electronics was 100 ns, much smaller than the width of the capture probability peak.

In addition to capture γ-ray pulses from the neutrons of interest, the photomultipliers could detect pulses from recoil protons produced by neutrons slowing down in the tank, from γ rays emitted from the sample, from neutrons produced in events other than the one of interest, and from background events such as decay of ^{40}K or radium in the shielding. Background subtraction will be described later. Pulses from delayed γ activity in the sample were not subtracted because they were difficult to identify, and their effect was assumed to be negligible. The other unwanted signals, mainly from prompt γ rays and recoil protons, were largely excluded by chopping the neutron beam and turning the detector off during the beam pulse. The beam was on for 1.0 μs with a pulse repetition rate of 25 kHz. The neutron counting gate started 0.5 μs after the end of the beam pulse and lasted 23 μs. The remaining 15.5 μs between beam pulses was used to process the data signals.

The arrival time of the neutron beam at the sample was determined by observing the current from the pulsed deuteron beam striking the edge of a 2-mm-diam collimator 20 cm in front of the tritium cell. Beam pulse intensities were kept low enough so that the results could be accurately corrected for more than one neutron-producing event in the sample during a pulse.

D. Detector efficiency

The efficiency of the scintillator tank for neutron detection depends mainly on the tank size, the counting gate length, and the photomultiplier discriminator thresholds. With a 75-cm-diam tank, efficiencies greater than 80% can be obtained with a counting gate of 30 to 40 μs and thresholds around 0.5 MeV. However, for this experiment the background rates under such conditions were too high. Reducing the efficiency to about 60% by shortening the gate and raising the thresholds lowered the background rate to less than 20% of what it was for 80% efficiency, making the measurements possible.

The efficiency for detecting prompt neutrons from spontaneous fission of ^{252}Cf was measured by placing the source, on a solid state detector, at the center of the tank and counting the number of neutrons from each fission event identified by the detector. The observed neutron multiplicities were corrected for deadtime losses and backgrounds, and the efficiency was determined by dividing the average multiplicity by 3.733, the number of prompt neutrons emitted per fission[7] by ^{252}Cf. The fission neutron spectrum of Green, Mitchel, and Steen[8] was used to correct this average efficiency for the effects of the difference in the energy spectra between the fission neutrons and the neutrons from the $(n,2n)$ or $(n,3n)$ reaction of interest. Statistical preequilibrium model calculations (described in Sec. IV) were used to obtain the first and second neutron spectra from $(n,2n)$ events and the first, second, and third neutron spectra from $(n,3n)$ reactions. An example

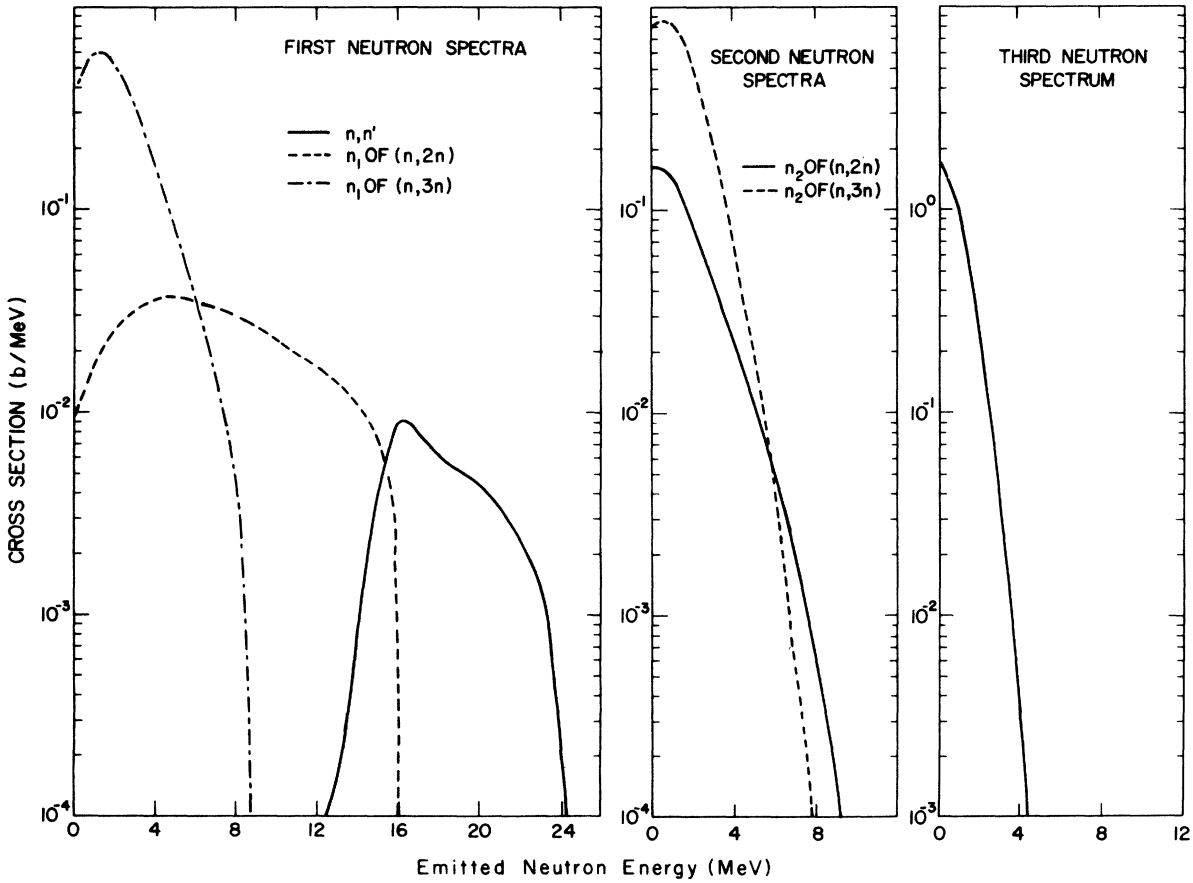

FIG. 3. Calculated first, second, and third neutron spectra for ^{197}Au(n,xn) reactions induced by 24-MeV neutrons. These spectra were used to make a small correction in the measured detector efficiency. The calculations are described in Sec. IV.

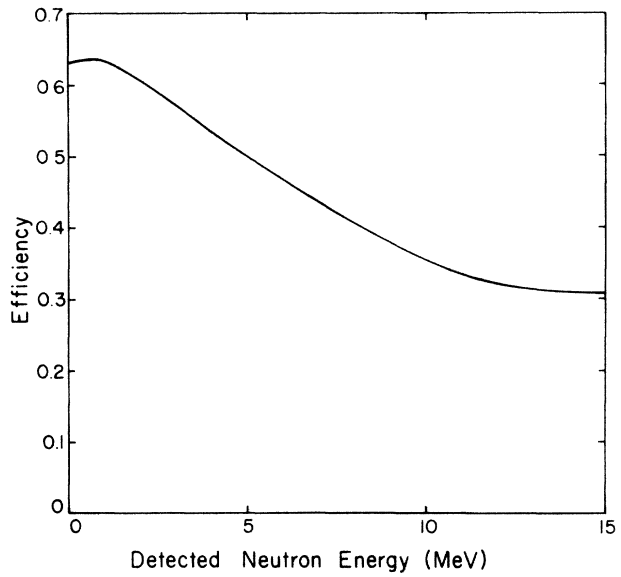

FIG. 4. Calculated detector efficiency versus the energy of the detected neutron. Calculations were made with the Monte Carlo code DENIS (see Ref. 9).

of the calculated spectra is shown in Fig. 3. The efficiency of the scintillator tank (see Fig. 4) was calculated as a function of the energy of the detected neutrons using a Monte Carlo code,[9] DENIS, which had been checked against measurements made by Boldeman[10] using a tank similar in size to ours. The corrected efficiency was determined by multiplying the measured efficiency by the ratio of the calculated efficiency for the reaction to that for ^{252}Cf neutrons. Usually the correction changed the measured efficiency by less than 5% of its value. However, for energies far above the $(n,3n)$ threshold, a large fraction of the $(n,2n)$ events produce high-energy neutrons, and the resulting corrections sometimes reduced the efficiency by as much as 25 to 30% at 24 MeV. The $(n,3n)$ spectra are softer, and in general the $(n,3n)$ efficiencies were slightly greater than the average efficiency for ^{252}Cf neutrons.

E. Samples

The samples were thin disks about 6 cm in diameter suspended in the neutron beam at the center of the tank. (The beam diameter there was 9 cm.) The scandium sample was a self-supporting oxide; all other samples were metallic. No correction was made for the oxygen in the scandium sample because the ^{16}O$(n,2n)$ cross section is small. When a sample consisted of more than one disk, the disks were spaced about 1 cm apart. The total thickness of each sample was chosen so that the total cross section times the number of atoms per unit area was about 0.02. Table I lists for each sample the isotopic composition, the total weight, and the number of disks used. No corrections were made to the data for multiple scattering in the samples, but a correction of about 1% was made for neutron beam attenuation. The ^{175}Lu and the ^{181}Ta results were not corrected for any contribution from other isotopes in the unenriched samples.

F. Measurements

The measurements for a given incident neutron energy involved a series of runs including at least one run for each sample, four or five background runs of similar length taken with the sample out, numerous short background runs made with the accelerator beam off, and a run with the ^{252}Cf source in the tank to check the efficiency. Beam intensities and focus conditions were kept relatively constant during the day so that the background subtraction and other corrections would be accurate. Interspersing the sample-out runs among the others provided a sensitive check on changes in the background conditions. Background rates with the beam off averaged 0.08 counts per opening of the counting gate, and the backgrounds with the beam on and the sample removed from inside the tank were 2 to 4 times larger. After subtraction of the beam-off background and application of the other corrections described in Sec. III, the number of beam-on, sample-out events with more than one pulse was small compared with the number of multiple-neutron events for a sample-in run. Thus it appears that almost none of the beam-induced background pulses were correlated.

An XDS-930 computer recorded the pulse height spectrum from the monitor detector, as well as the output from a scaler measuring the integrated current of deuterons striking the tritium cell. (The current integration was used to check that the

TABLE I. Target characteristics.

Target	Isotopic composition (%)		Weight (g)	Number of disks
Scandium	$^{45}Sc_2O_3$	100	15.05	2
Cobalt	^{59}Co	100	10.93	2
Yttrium	^{89}Y	100	14.61	2
Niobium	^{93}Nb	100	17.50	2
Rhodium	^{103}Rh	100	33.04	1
Thulium	^{169}Tm	100	30.85	3
Lutetium	^{175}Lu	97.41	34.97	2
	^{176}Lu	2.59		
Tantalum	^{181}Ta	99.99	43.91	2
	^{180}Ta	0.0123		
Gold	^{197}Au	100	35.18	2
Bismuth	^{209}Bi	100	42.53	2

beam focus, tritium pressure, etc., remained constant from one run to the next.) A fast scaler counted the number of tank pulses during each counting gate, and the computer sorted the events according to the number of neutrons detected. An on-line analysis program subtracted the backgrounds and did the other calculations to determine the cross sections.

III. DATA ANALYSIS

A small correction was applied to each run, including backgrounds, to account for any loss of tank pulses because of coincidences during the 100-ns deadtime associated with each neutron pulse. Then the sample-out background runs from a series of runs at one energy were combined and subtracted from each of the cross-section runs. Equations describing the deadtime correction and the background subtraction are given in Ref. 11.

For some of the runs the number of scattered neutrons was large enough that the probability of two single-neutron events occurring during the same pulse was not negligible compared with the number of $(n,2n)$ events. An appropriate multiple-events correction[5] was applied to all of the sample-in runs. For $(n,3n)$ measurements the correction was negligible and for $(n,2n)$ it was up to 10% ($\leq$40% for scandium which had more scattering because of oxygen in the sample). To check the accuracy of the multiple-events correction, we made several runs with a carbon sample for which the $(n,2n)$ cross section is very small and observed that the corrected number of multiple events was always negligible. We also repeated runs for many energies and samples using a lower beam intensity to check for reproducibility of the measurements.

The final correction to the results removed the effects of detector efficiency to give the multiplicities of neutrons emitted from the sample. Because $(n,2n)$ reactions and $(n,3n)$ reactions produce different spectrum shapes and therefore different detector efficiencies, it is necessary to include both efficiency values in the equations. We assume that C_i is the probability of detecting i neutrons per event, P_n is the probability of emission of n neutrons per event, and ϵ_n is the average efficiency for detecting the neutrons from an event in which n neutrons are emitted. Then

$$C_i = \sum_{n=i}^{\infty} \frac{n!}{i!\,(n-i)!} \epsilon_n^i (1-\epsilon_n)^{n-i} P_n .$$

Because the measurements were made below the $(n,4n)$ threshold, $P_n = 0$ for $n \geq 4$. Therefore

$$C_3 = \epsilon_3^3 P_3$$

and

$$C_2 = \epsilon_2^2 P_2 + 3\epsilon_3^2 (1-\epsilon_3) P_3 .$$

Inverting gives

$$P_3 = C_3/\epsilon_3^3$$

and

$$P_2 = [C_2 - 3C_3(1-\epsilon_3)/(\epsilon_3]/\epsilon_2^2 .$$

The largest uncertainty in the measurements was the statistical uncertainty in the measured numbers of events producing zero, one, two, or three neutrons or similar numbers of background counts. The statistical uncertainty in the multiple-events correction was relatively small. The deadtime correction was also small for this experiment, where multiplicities higher than three were not used, and its uncertainty was assumed to be 10% of the correction. The uncertainty in ϵ_n was assumed to be 0.01 for all measurements. The uncertainty in $\bar{\nu}$ for the ^{252}Cf standard caused an uncertainty in ϵ_n of 0.0013, and the statistical uncertainty in measuring ϵ_n for a series of runs was generally around 0.004. The uncertainty in the correction for the difference in spectra for ^{252}Cf fission neutrons and those for $(n,2n)$ and $(n,3n)$ reactions is difficult to estimate accurately. Since the correction was usually 0.03 or less (see Sec. II), a value of 0.01 for the total uncertainty in ϵ_n seems reasonable for most of the measurements. Where the $(n,2n)$ cross section was small and the $(n,3n)$ cross section large, the correction to ϵ_2 was often larger than 0.03, but for simplicity we assumed $\Delta\epsilon = 0.01$ because the large (20–40%) statistical uncertainties for these points made $\Delta\epsilon_2$ relatively insignificant.

IV. MODEL CALCULATIONS

Cross-section calculations, based on a statistical model, were made to investigate the inclusion of preequilibrium effects in the model as well as the use of comprehensive parameter sets to describe the level densities in the nucleus and the optical models from which transmission coefficients are derived. The calculations also gave the complex neutron spectra (see Fig. 3) used to estimate the detector efficiency corrections described in Sec. II.

The statistical portion of the calculations included angular momentum and parity effects explicitly and followed the formalism described by Uhl.[12] Decay chains involving up to 10 compound nuclei could be followed, and each compound system was allowed to emit γ rays and a neutron, a proton, or an α particle. The γ-ray cascades were followed in detail.

In the calculation of (n,xn) reactions, where several emitted particles and compound nuclei are involved, it was assumed that the reaction proceeds in stages with only one particle emitted at each step and that each newly formed intermediate nucleus, produced by particle decay of the previous compound system, disintegrates with probabilities determined from Hauser-Feshbach theory for binary reactions.[13] At low excitation energies, each nucleus in the calculation was composed of discrete levels having energy E, total angular momentum J, and parity π; we used experimentally determined values for E, J, and π. The higher excitation energy region, where information concerning discrete levels was not known, was represented by a continuum level density expression.

The population of continuum bins $P^{(n+1)}(UJ\pi)$ in the $(n+1)$th compound nucleus, formed by particle disintegration of the nth compound nucleus, is given by

$$P^{(n+1)}(UJ\pi)=\int dU' \sum_{J'\pi'} \hat{P}^{(n)}(U'J'\pi') \frac{\Gamma_a^{(n)}(U'J'\pi', UJ\pi)}{\Gamma(U'J'\pi')} \times \rho^{(n+1)}(UJ\pi), \quad (1)$$

where $\hat{P}^{(n)}(U'J'\pi')$ is the population of continuum energy bins in the nth compound nucleus after γ-ray cascades have been considered. The population of the first compound nucleus is determined from its formation cross section, which can be found from the appropriate sum over transmission coefficients taken at the center-of-mass energy, $\mathcal{E}$, of the incident particles,

$$P^{(1)}(UJ\pi)=\frac{\pi}{k^2}\frac{(2J+1)}{(2I+1)(2i+1)}\sum_s\sum_l T_l(\mathcal{E})\delta(U-\mathcal{E}-B_a). \quad (2)$$

Here k is the relative motion wave number, I and i are the spins of the target nucleus and projectile, and J is the total angular momentum of the compound system. Other quantities appearing in Eqs. (1) and (2) are the level density ρ, transmission coefficients T_l, the binding energy B_a of the emitted particle a, and the excitation energies U and U' in the $(n+1)$th and nth compound nuclei, respectively. The partial decay widths used in Eq. (1) for reaction channel a have the general form

$$\Gamma_a^{(n)}(U'J'\pi', UJ\pi)=\frac{1}{2\pi\rho(U'J'\pi')}\sum_s\sum_l T_l(U'-U-B_a) \quad (3)$$

for widths involving transitions from continuum bins in the compound nucleus to continuum bins in the residual nucleus.

Similar expressions hold for the population of discrete levels:

$$P^{(n+1)}(E_\lambda J_\lambda \pi_\lambda) = \int dU' \sum_{J'\pi'} \hat{P}^{(n)}(U'J'\pi') \frac{\Gamma_a^{(n)}(U'J'\pi', E_\chi J_\lambda \pi_\lambda)}{\Gamma(U'J'\pi')}, \quad (4)$$

where the partial width for continuum to discrete level transition has the form

$$\Gamma_a(U'J'\pi', E_\chi J_\lambda \pi_\lambda)=\sum_s\sum_l T_l(U'-E_\lambda-B_a). \quad (5)$$

Here the sums are taken over channel spin s and orbital angular momentum l. The total width appearing in the denominator of Eqs. (1) and (4) is then the sum over continuum bins $(UJ\pi)$ or discrete levels $(E_\chi J_\lambda \pi_\lambda)$ of the appropriate partial width $\Gamma_a(U'J'\pi', UJ\pi)$ or $\Gamma_a(U'J'\pi', E_\chi J_\lambda \pi_\lambda)$ for each reaction channel a.

In these calculations we used transmission coefficients T_l calculated with "global" sets of optical model parameters; that is, sets that fit measurements for a variety of nuclei over a range of incident energies. For neutrons these were the Wilmore-Hodgson parameters,[14] for protons the parameters of Perey,[15] and for α particles the McFadden-Satchler[16] parameters or other values compiled in Ref. 17 for the particular nucleus of interest.

For γ-ray reduced widths we used the Brink-Axel giant dipole resonance form.[18] The reduced widths were normalized to the ratio of the γ-ray width to the observed level spacing obtained from s-wave neutron capture. We also allowed γ-ray emission by $M1$ and $E2$ transitions; the ratios of these strengths to the $E1$ strength were obtained from the Weisskopf single-particle estimate.[19]

The continuum energy region of each nucleus was represented by the Gilbert-Cameron level density expression[20] with the pairing and shell parameters of Cook.[21] In this expression a Fermi gas form was used at higher excitation energies, but at lower energies a constant temperature expression, adjusted to fit level parameters for each individual nucleus, was used.

Previous studies of $(n,2n)$ and $(n,3n)$ reactions have shown preequilibrium effects to be important,[4,22] particularly at high incident energies. In the preequilibrium formalism the initial interaction produces a simple two-particle, one-hole configuration that then proceeds through a series of increasingly more complicated states until the compound nuclear state (equilibrium) is reached. Each intermediate system has some probability for emitting a particle. Thus, the secondary neutron spectrum for (n,xn) reactions includes preequilibrium neutrons in addition to the neutrons produced by compound nuclear decays. Because the preequilibrium neutrons usually have more energy, the chance of further neutron emissions is

TABLE II. $(n,2n)$ cross sections (in barns).

E_n (MeV)	^{45}Sc	^{59}Co	^{89}Y	^{93}Nb	^{103}Rh	^{169}Tm	^{175}Lu	^{181}Ta	^{197}Au	^{209}Bi
14.7±0.15	0.331±0.024	0.820±0.085	1.029±0.055	1.279±0.088	1.427±0.079	1.811±0.111	1.984±0.115	2.122±0.115	2.064±0.125	2.180±0.103
16.0±0.20	0.473±0.035	0.838±0.055	1.185±0.064	1.433±0.076	1.434±0.068	1.883±0.105	1.992±0.105	1.882±0.086	2.148±0.101	2.294±0.125
17.0±0.20	0.514±0.037	0.840±0.056	1.222±0.067	1.300±0.072	1.461±0.070	1.906±0.096	1.787±0.085	1.567±0.061	2.031±0.092	2.148±0.104
18.0±0.15	0.489±0.035	0.832±0.054	1.207±0.066	1.337±0.097	1.446±0.081	1.524±0.098	1.320±0.088	1.320±0.081	1.692±0.087	1.620±0.100
19.0±0.15	0.533±0.032	0.862±0.047	1.209±0.061	1.265±0.065	1.356±0.066	1.084±0.061	0.957±0.064	0.905±0.062	1.223±0.055	1.274±0.060
20.0±0.11	0.523±0.033	0.910±0.053	1.261±0.066	1.194±0.085	1.217±0.066	0.974±0.098	0.770±0.104	0.758±0.093	0.904±0.130	1.020±0.105
21.0±0.12	0.504±0.036	0.773±0.049	1.214±0.066	0.933±0.051	0.965±0.042	0.772±0.073	0.722±0.068	0.646±0.081	0.795±0.074	0.831±0.089
22.0±0.10	0.490±0.031	0.673±0.060	1.156±0.059	0.708±0.051	0.763±0.048	0.614±0.100	0.535±0.079	0.489±0.110	0.679±0.074	0.466±0.129
23.0±0.07	0.450±0.033	0.608±0.068	1.105±0.083	0.602±0.077	0.695±0.053	0.545±0.098	0.562±0.098	0.574±0.115	0.487±0.102	0.606±0.136
24.0±0.06	0.361±0.053	0.674±0.098	1.042±0.105	0.483±0.124	0.495±0.072	0.346±0.163	0.524±0.154	0.406±0.145	0.434±0.151	0.409±0.189

TABLE III. $(n,3n)$ cross sections (in barns).

E_n (MeV)	^{59}Co	^{89}Y	^{93}Nb	^{103}Rh	^{169}Tm	^{175}Lu	^{181}Ta	^{197}Au	^{209}Bi
16.0±0.20					0.070±0.027	0.147±0.027	0.261±0.023	0.065±0.016	0.127±0.029
17.0±0.20					0.241±0.026	0.455±0.034	0.620±0.039	0.210±0.020	0.357±0.030
18.0±0.15			0.031±0.029	0.028±0.018	0.516±0.046	0.699±0.053	0.836±0.058	0.424±0.036	0.596±0.048
19.0±0.15			0.132±0.016	0.140±0.015	0.892±0.056	1.099±0.067	1.188±0.071	0.870±0.054	1.042±0.066
20.0±0.11			0.179±0.028	0.204±0.021	1.059±0.074	1.226±0.082	1.352±0.086	1.107±0.081	1.237±0.082
21.0±0.12	0.021±0.011		0.341±0.025	0.374±0.025	1.216±0.074	1.295±0.077	1.408±0.085	1.271±0.078	1.415±0.087
22.0±0.10	0.039±0.015	0.028±0.009	0.526±0.037	0.528±0.035	1.319±0.083	1.405±0.090	1.551±0.095	1.412±0.089	1.612±0.101
23.0±0.07	0.081±0.020	0.060±0.022	0.576±0.042	0.644±0.042	1.389±0.094	1.421±0.096	1.520±0.094	1.545±0.100	1.569±0.099
24.0±0.06	0.112±0.030	0.080±0.033	0.756±0.062	0.777±0.051	1.551±0.100	1.572±0.100	1.604±0.100	1.587±0.102	1.800±0.116

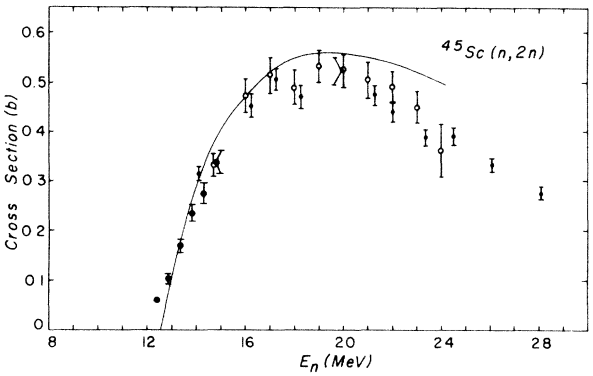

FIG. 5. Cross sections for ^{45}Sc$(n,2n)^{44}$Sc. The large closed circles are from Ref. 3, the small closed circles are from Ref. 4, the open circles are our measurements and the lines are calculated values.

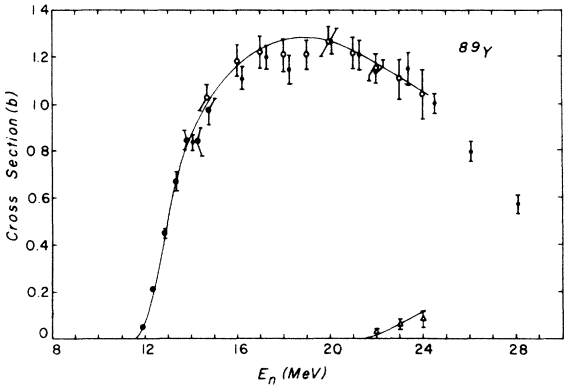

FIG. 7. Cross sections for ^{89}Y(n,xn). The large closed circles are from Ref. 3, the small closed circles are from Ref. 4, the open circles are our $(n,2n)$ results, the open triangles are our $(n,3n)$ results, and the lines are calculated values.

decreased compared with the case where the first emitted neutron is from the compound system. Consequently, for the highest energies of our measurements, the $(n,2n)$ cross section tends to be increased and the $(n,3n)$ cross section decreased relative to the predictions of the statistical model.

We included preequilibrium neutron emission using an expression based on the exciton model of Griffin[23] and Blann[24]

$$\left(\frac{d\sigma}{d\epsilon}\right)_{\text{preq}} \propto \frac{\sigma_{\text{inv}}(\epsilon) m \epsilon \sigma_R}{|M|^2 g^4 E^3} \sum_{n=3}^{\bar{n}} (U/E)^{n-2}(n+1)^2(n-1) . \tag{6}$$

In this expression, E and U are the excitation energies of the compound and residual nuclei, respectively; σ_R is the neutron reaction cross section; m, ϵ, and $\sigma_{\text{inv}}(\epsilon)$ are the mass, kinetic energy, and inverse cross section for the outgoing particle; g is the average single particle level spacing from the Fermi gas model; and n is the number of particles and holes $(n = p + h)$ in the compound nucleus. The sum extends from the initial exciton number (here assumed to be 3) to $\bar{n}$, the limiting value obtained when equilibrium is reached.

The absolute square of the average matrix element of residual two-body interactions, $|M|^2$, was assumed to have the form $|M|^2 = KA^{-3}E^{-1}$ as determined by Kalbach-Cline.[25] The normalization constant K was obtained from fits to various sets of experimental data for neutron-induced reactions[26,27] including both spectra and integrated cross sections. A value of 150 MeV^3 was obtained for K, in agreement with values determined in

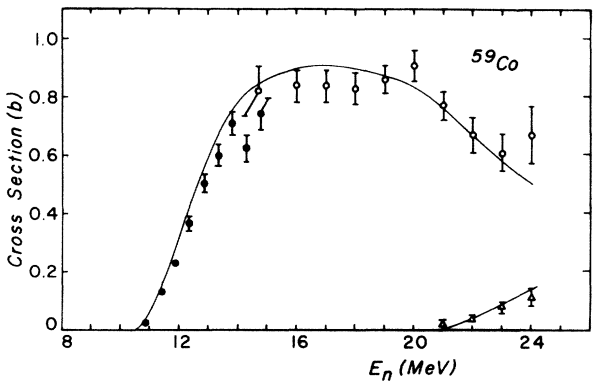

FIG. 6. Cross sections for ^{59}Co(n,xn). The closed circles are from Ref. 3, the open circles are our $(n,2n)$ results, the open triangles are our $(n,3n)$ results, and the lines are calculated values.

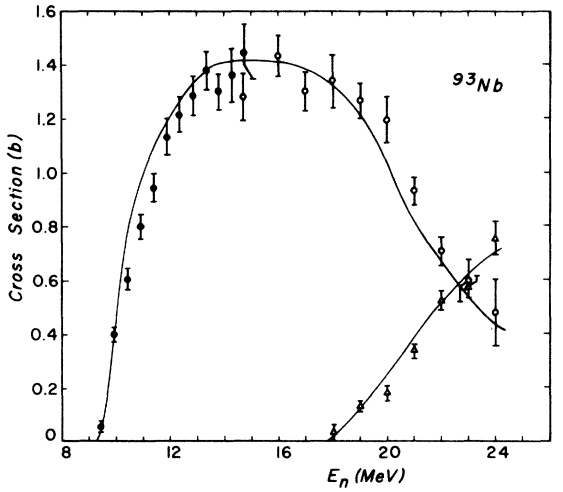

FIG. 8. Cross sections for ^{93}Nb(n,xn). The closed circles are from Ref. 3, the open circles are our $(n,2n)$ results, the open triangles are our $(n,3n)$ results, and the lines are calculated values.

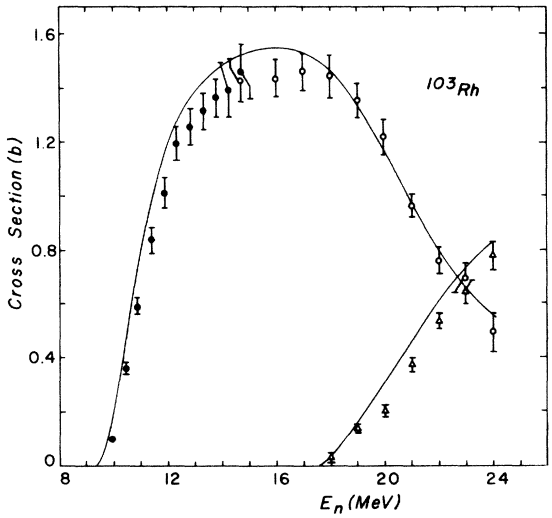

FIG. 9. Cross sections for ^{103}Rh(n,xn). The closed circles are from Ref. 3, the open circles are our $(n,2n)$ results, the open triangles are our $(n,3n)$ results, and the lines are calculated values.

Refs. 25 and 26. The preequilibrium component calculated with Eq. (6) was used to renormalize the statistical-model populations of Eqs. (1) and (4). Because the preequilibrium model does not include effects of spin and parity, we assumed that the preequilibrium component would have the same spin and parity distribution as the statistical population component.

V. EXPERIMENTAL RESULTS

The results of the $(n,2n)$ measurements are listed in Table II and the $(n,3n)$ results are in Table III. The uncertainty given for each measurement includes the statistical uncertainty (standard deviation), the uncertainty in the corrections, an

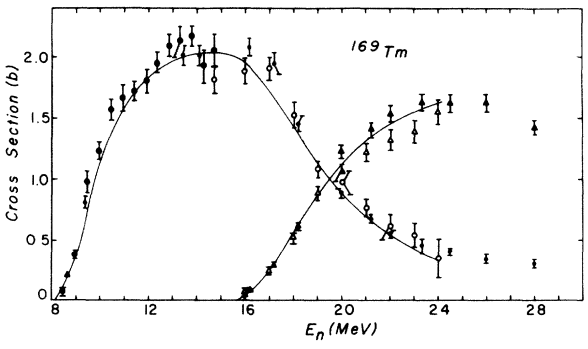

FIG. 10. Cross sections for ^{169}Tm(n,xn). The large closed circles are from Ref. 3, the small closed circles and the closed triangles are from Ref. 4, the open circles are our $(n,2n)$ results, the open triangles are our $(n,3n)$ results, and the lines are calculated values.

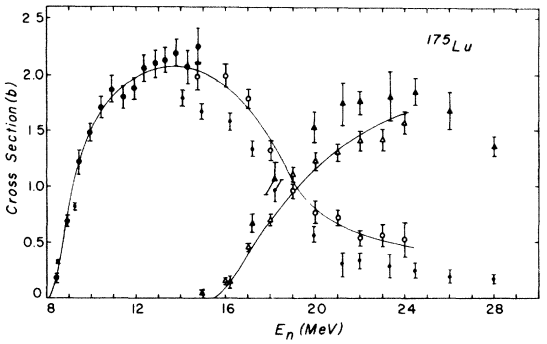

FIG. 11. Cross sections for ^{175}Lu(n,xn). The large closed circles are from Ref. 3, the small closed circles and the closed triangles are from Ref. 4, the open circles are our $(n,2n)$ results, the open triangles are our $(n,3n)$ results, and the lines are calculated values.

uncertainty of $\Delta\epsilon = 0.01$ in the detector efficiency, and an estimated uncertainty of ±3% in the neutron flux determination. The results are also plotted in Figs. 5–14, along with some results of previous measurements and curves showing the model calculations. Round symbols are the $(n,2n)$ measurements and triangles show the $(n,3n)$ cross sections. The open symbols are values from this experiment, the larger closed round symbols show the measurements of Frêhaut and Mosinski[3] made with a scintillator tank and neutrons from the ^{2}H(d,n)-^{3}He reaction, and the other points are radiochemical results.[4]

The $(n,2n)$ measurements tend to agree quite well with other experimental results, but we find some systematic differences of up to 15% between our $(n,3n)$ results and those of Bayhurst.[4] An exception occurs for the lutetium cross sections where there is a larger disagreement of radio-

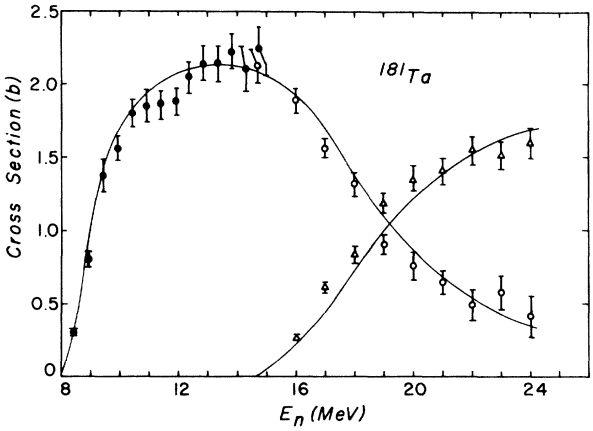

FIG. 12. Cross sections for ^{181}Ta(n,xn). The closed circles are from Ref. 3, the open circles are our $(n,2n)$ results, the open triangles are our $(n,3n)$ results, and the lines are calculated values.

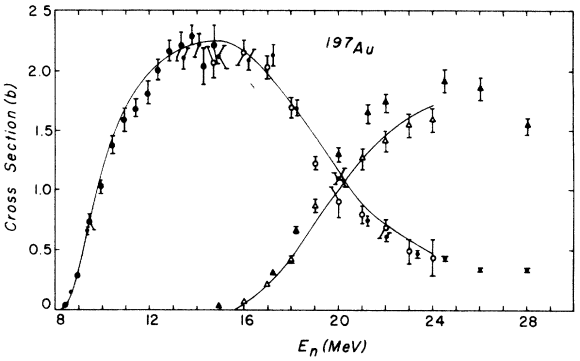

FIG. 13. Cross sections for ^{197}Au(n,xn). The large closed circles are from Ref. 3, the small closed circles and the closed triangles are from Ref. 4, the open circles are our $(n,2n)$ results, the open triangles are our $(n,3n)$ results, and the lines are calculated values.

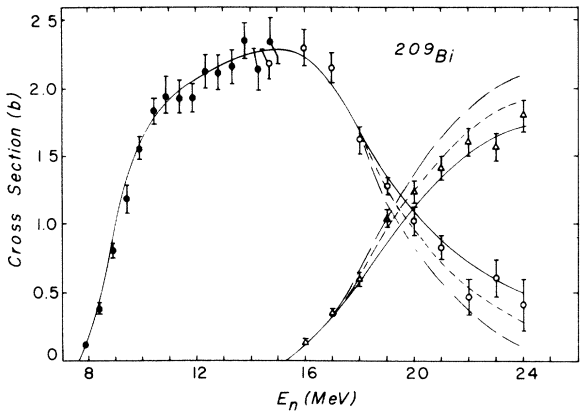

FIG. 14. Cross sections for ^{209}Bi(n,xn). The closed circles are from Ref. 3, the open circles are our $(n,2n)$ results, the open triangles are our $(n,3n)$ results, and the lines are calculated values. The curves with long dashes were calculated using no preequilibrium effects, the curves with short dashes were calculated with a preequilibrium effect depending on mass, and the solid curves are for a preequilibrium effect normalized to both mass and excitation energy.

chemical results with our measurements and the calculated cross sections. This disagreement may be explained by the fact that radiochemical measurements for lutetium are difficult because of the nature of the half-lives and decay schemes of the nuclei involved and because of a background from the decay of the naturally occurring radioactive isotope ^{176}Lu.

The comparison of the calculated curves shows general agreement with the experimental data. As described in Sec. IV, these calculations were made with transmission coefficients generated from global optical model sets and with generalized level density parameter sets. In some cases, minor adjustments were made in the normalization of the reduced γ ray width to better reproduce cross-section shapes near $(n,2n)$ and $(n,3n)$ thresholds. In these energy regions, especially for heavier nuclei where only γ ray emission competes with neutron emission, the threshold shape is relatively sensitive to the γ ray strength used. For lighter nuclei it was necessary to include competition from proton and α-particle emission to reproduce the threshold (n,xn) shape.

In Fig. 14 the effects of the inclusion of preequilibrium emission and of changes in the form of the normalization of the matrix term $|M|^2$ in Eq. (6) are shown for ^{209}Bi(n,xn) reactions. The calculations without preequilibrium (long-dashed curve), as well as those with matrix element $|M|^2$ having only an A^{-3} dependence (short-dashed curve) fail to reproduce the measured cross sections at high energies. The solid curve represents the calculation made with $|M|^2 = KA^{-3}E^{-1}$. The calculations shown in Figs. 5–13 were made with this form of $|M|^2$. These calculations, which include preequilibrium effects and competition from γ-ray and charged-particle emission and which use global input parameter sets, appear to reproduce the experimental results adequately.

ACKNOWLEDGMENTS

We wish to thank C. E. Moss for keeping the accelerator operable and J. Fréhaut and B. C. Diven for their help and advice in carrying out the experiment.

†Work performed under the auspices of the U.S. ERDA.

[1]V. J. Ashby, H. C. Catron, L. L. Newkirk, and C. J. Taylor, Phys. Rev. 111, 616 (1958).

[2]D. S. Mather, P. F. Bampton, R. E. Coles, G. James, and P. J. Nind, Atomic Weapons Research Establishment Report No. AWRE 0 72/72 (H. M. Stationery Office, London, 1972).

[3]J. Fréhaut and G. Mosinski, in *Nuclear Cross Sections and Technology* (National Bureau of Standards special publication 425, U.S. Government Printing Office, 1975), p. 855; in, Proceedings of the National Soviet Conference on Neutron Physics, Kiev, 1975 (unpublished).

[4]B. P. Bayhurst, J. S. Gilmore, R. J. Prestwood, J. B. Wilhelmy, N. Jarmie, B. H. Erkkila, and R. A. Hardecopf, Phys. Rev. C 12, 451 (1975).

[5]J. Fréhaut, Nucl. Instrum. Methods 135, 511 (1976).

[6]V. V. Verbinski, W. R. Burrus, T. A. Love, W. Zobel, and N. W. Hill, Nucl. Instrum. Methods 65, 8 (1968).

[7]Neutron Standard Reference Data (IAEA, Vienna, 1974),

p. 360.
[8]L. Green, J. A. Mitchel, and N. M. Steen, Nucl. Sci. Eng. 50, 257 (1973).
[9]J. Poitou and C. Signarbieux, Nucl. Instrum. Methods 114, 113 (1974).
[10]J. W. Boldeman, Nucl. Sci. Eng. 55, 188 (1974).
[11]B. C. Diven, H. C. Martin, R. F. Taschek, and J. Terrell, Phys. Rev. 101, 1012 (1956).
[12]M. Uhl, Acta Phys. Austriaca 31, 245 (1970).
[13]W. Hauser and H. Feshbach, Phys. Rev. 87, 366 (1952).
[14]D. Wilmore and P. E. Hodgson, Nucl. Phys. 55, 673 (1964).
[15]F. G. Perey, Phys. Rev. 131, 745 (1963).
[16]L. McFadden and G. R. Satchler, Nucl. Phys. 84, 177 (1966).
[17]C. M. Perey and F. G. Perey, At. Data Nucl. Data Tables 13, 293 (1974).
[18]D. M. Brink, Ph.D. thesis, Oxford University, 1955; P. Axel, Phys. Rev. 126, 671 (1962).
[19]J. M. Blatt and V. F. Weisskopf, *Theoretical Nuclear Physics* (Wiley, New York, 1952), p. 627.
[20]A. Gilbert and A. G. W. Cameron, Can. J. Phys. 43, 1446 (1965).
[21]J. L. Cook, H. Ferguson, and A. R. de L. Musgrove, Aust. J. Phys. 20, 477 (1967).
[22]E. Holub and N. Cindro, Phys. Lett. 56B, 143 (1975).
[23]J. J. Griffin, Phys. Rev. Lett. 17, 478 (1966).
[24]M. Blann, Phys. Rev. Lett. 21, 1357 (1968).
[25]C. Kalbach-Cline, Nucl. Phys. A210, 590 (1973).
[26]G. M. Braga-Marcazzan, E. Gadioli-Erba, L. Milazzo-Colli, and P. G. Sona, Phys. Rev. C 6, 1398 (1972).
[27]For example, see D. Hermsdorf, S. Sassonoff, D. Seeliger, and K. Seidel, Technical University of Dresden Report No. ZFK-277, 1974 (unpublished); S. M. Grimes, R. C. Haight, and J. D. Anderson, Lawrence Livermore Laboratory Report No. UCRL-78314, 1976 (unpublished).

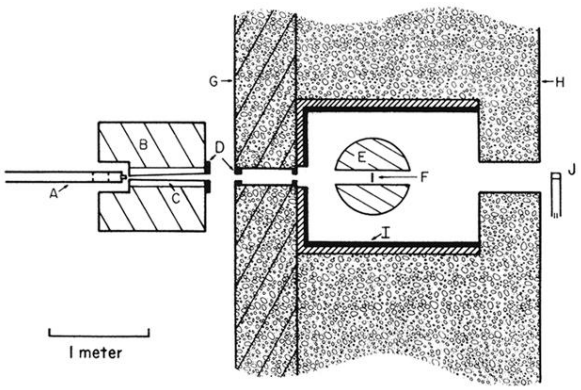

FIG. 1. The experimental arrangement: (A) accelerator beam tube, collimator, and tritium cell; (B) iron shield; (C) brass neutron collimator; (D) boron shielding; (E) scintillator tank; (F) sample; (G) magnetite concrete shielding; (H) gypsum shielding; (I) borax and lead shielding layers; (J) neutron monitor detector.